Investigation of Geometries of Bistable Piezoelectric-Laminate Plates for Vibration-based Energy Harvesting

David N. Betts*[a], Christopher R. Bowen[a], Daniel J. Inman[b], Paul M. Weaver[c], H. Alicia Kim[a]
[a]Department of Mechanical Engineering, University of Bath, Bath, BA2 7AY, UK;
[b]Department of Aerospace Engineering, University of Michigan, Ann Arbor, MI, 48109, USA;
[c]National Physical Laboratory, Teddington, TW11 0LW, UK

ABSTRACT

The need for reduced power requirements for small electronic components, such as wireless sensor networks, has prompted interest in recent years for energy harvesting technologies capable of capturing energy from broadband ambient vibrations. Encouraging results have been reported for an arrangement of piezoelectric layers attached to carbon fiber / epoxy laminates which possess bistability by virtue of their specific asymmetric stacking sequence. The inherent bistability of the underlying structure is exploited for energy harvesting since a transition from one stable configuration to another, or 'snap-through', is used to repeatedly strain the surface-bonded piezoelectric and generate electrical energy. Existing studies, both experimental and modelling, have been limited to simple geometric laminate shapes, restricting the scope for improved energy harvesting performance by limiting the number of design variables. In this paper we present an analytical model to predict the static shapes of laminates of any desired profile, validated experimentally using a digital image correlation system. Good accuracy in terms of out-of-plane displacements (5-7%) are shown in line with existing square modelling results. The static model is then mapped to a dynamics model and used to compare results against an experimental study of the harvesting performance of an example arbitrary geometry piezoelectric-laminate energy harvester.

Keywords: Bistable laminates, piezoelectric, energy harvesting, broadband.

1. INTRODUCTION

Vibration-based energy harvesting for low-powered electronics has received significant interest in recent years as solutions are sought to provide remote sources of power for applications such as wireless sensor networks or safety monitoring devices. While energy harvesters are often tuned to operate near resonance, many typical vibration patterns are composed of multiple frequencies across a wide band[1-3]. For efficient energy harvesting it is therefore necessary to tune the operating frequencies, typically achieved through geometry and mass variation, and to broaden the frequency bandwidth by introducing stiffness nonlinearities, typically achieved through the use of external magnets[4]. A solution which allows design for both mass distribution and specific nonlinear stiffness characteristics through variation in geometric variables is desirable. One approach is to exploit bistability in composite laminates with an asymmetric stacking sequence. The advantage of this approach is that it removes the need for external components. It is well known that composite laminates with asymmetric stacking sequences may exhibit two curved stable shapes due to the mismatch in thermal properties between plies and the temperature change experienced during manufacture[5]. This property makes them suitable for piezoelectric energy harvesting by utilising a snap-through mechanism between the two stable states to repeatedly strain a surface-bonded piezoelectric, such as a Macro Fibre Composite (MFC).

Significant power outputs over a wide bandwidth have been reported using square bistable laminates[6]. The full potential for improving the power generation of bistable laminate energy harvesters and to reduce the mechanical energy input required to induce snap-through has yet to be exploited since existing designs have been limited to square and rectangular laminate shapes[6-8].

Static modelling of the stable shapes of square bistable laminates is well established[5,9], in which the curved shapes of asymmetric laminates due to the high temperatures experienced during manufacturing (curing process) are modelled based on a nonlinear extension to classical laminated plate theory. The midplane strains and out-of-plane displacement profile are assumed to conform to second order polynomials. The process of identifying the static stable shapes is performed by identifying the values of the coefficients of these assumed polynomials through minimisation of the total

*D.N.Betts@bath.ac.uk; phone +44 (0)1225 385558; fax +44 (0)1225 386928.

strain energy. This modelling approach has been validated experimentally and using finite element analysis for square and rectangular laminates[9-11]. We have previously mapped this static modelling to a dynamics model including piezoelectric elements for energy harvesting by characterising the double-well restoring force of the device as a function of displacements about the static shapes[12]. This model provides a prediction of power outputs for any given vibration pattern, captures the full range of dynamic modes seen experimentally, and the boundaries between these modes, limited to square laminates. The cured shapes of bistable laminates of trapezoidal and triangular planform have been considered experimentally and modelled using finite element analysis[13] for morphing applications, and have been modelled analytically in tapered cantilever configurations[14]. However, to date, no analytical model of the stable shapes of any profile, referred to in this work as 'arbitrary geometry' laminates, has been presented.

Figure 1 shows an example arbitrary geometry laminate centrally mounted on an electrodynamic shaker. Attached to the back surface of the laminate is a square piezoelectric MFC positioned at the centre. Vibration at sufficiently high acceleration induces snap-through between the two stable configurations, overlaid in Fig. 1. In this paper we present a modelling extension to the Ritz method to determine the stable laminate shapes for arbitrary planforms such as that shown in Fig. 1, including piezoelectric elements bonded to the laminate surface. This is achieved through discretisation of the planform by a grid of square elements to approximate the desired laminate shape. The static modelling of arbitrary geometry laminates is experimentally validated using a digital image correlation system to compare the out-of-plane displacements of a series of laminate designs against modelling predictions. The static modelling is then extended to a dynamics model including electromechanically coupled behaviour to predict the power outputs for base excited energy harvesting.

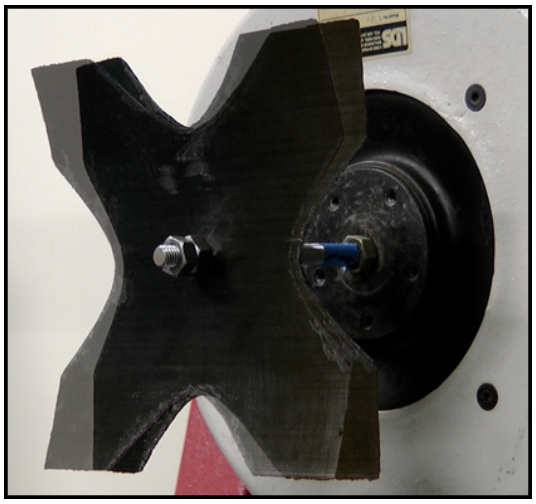

Figure 1. Two stable shapes (overlaid) of a single arbitrary shaped $[0/90]_T$ laminate. Overall laminate dimensions are 150 × 150 × 0.5mm. A piezoelectric element is attached to the back surface of the laminate.

2. A MODEL FOR BISTBLE PIEZOELECTRIC-LAMINATES OF ARBITRARY SHAPE

An existing model for prediction of the cured shapes of rectangular laminates of asymmetric layup with bonded piezoelectric elements is briefly outlined in the following section and subsequently extended for prediction of the static shapes of laminates of arbitrary planform. Finally, the nonlinear restoring force associated with deformation of the arbitrary geometry laminates about the static positions is mapped to a dynamics model to predict the response to base excitation for energy harvesting applications.

2.1 Static shapes of rectangular laminates

The model outlined in this section is based on that presented by Dano and Hyer[9]. The curved shapes of bistable cross-ply (e.g. $[0/90]_T$) laminates are assumed to conform to an out-of-plane displacement profile w, defined by two constant curvature coefficients, a and b.

$$w = \frac{1}{2}\left(ax^2 + by^2\right). \tag{1}$$

This out-of-plane profile results in in-plane displacements which are described by coefficients $d_{1\text{-}11}$. The resulting midplane strains are defined as,

$$\begin{aligned}
\varepsilon_x^0 &= \frac{\partial u^0}{\partial x} + \frac{1}{2}\left(\frac{\partial w}{\partial x}\right)^2 \\
\varepsilon_y^0 &= \frac{\partial v^0}{\partial y} + \frac{1}{2}\left(\frac{\partial w}{\partial y}\right)^2 \\
\varepsilon_{xy}^0 &= \frac{\partial u^0}{\partial y} + \frac{\partial v^0}{\partial x} + \frac{\partial w}{\partial x}\frac{\partial w}{\partial y}
\end{aligned} \tag{2}$$

where geometrical nonlinearity is included according to the von Karman hypothesis. The total strain energy due to thermal effects during the temperature change from the elevated cure temperature then takes the form,

$$W_{lam} = \frac{1}{2}\int_{-Ly/2}^{Ly/2}\int_{-Lx/2}^{Lx/2}\left[\begin{Bmatrix}\mathbf{N}\\ \mathbf{M}\end{Bmatrix} - \begin{Bmatrix}\mathbf{N^T}\\ \mathbf{M^T}\end{Bmatrix}\right]^T \begin{Bmatrix}\boldsymbol{\varepsilon}^{\mathbf{0}}\\ \boldsymbol{\kappa}^{\mathbf{0}}\end{Bmatrix} dxdy \tag{3}$$

where L_x and L_y are the edge-lengths of the laminate, **N** and **M** are vectors of forces and moments acting on the laminate,

$$\begin{Bmatrix}\mathbf{N}\\ \mathbf{M}\end{Bmatrix} = \begin{bmatrix}\mathbf{A} & \mathbf{B}\\ \mathbf{B} & \mathbf{D}\end{bmatrix}\begin{Bmatrix}\boldsymbol{\varepsilon}^{\mathbf{0}}\\ \boldsymbol{\kappa}^{\mathbf{0}}\end{Bmatrix} - \begin{Bmatrix}\mathbf{N^T}\\ \mathbf{M^T}\end{Bmatrix}^T \tag{4}$$

expressed in terms of the in-plane (**A**), coupling (**B**) and bending (**D**) stiffness matrices of the laminate, $\boldsymbol{\varepsilon}^0$ and $\boldsymbol{\kappa}$ are vectors of the strains $\{\varepsilon_x^0\ \varepsilon_y^0\ \varepsilon_{xy}^0\}$ and curvatures $\{a\ b\ 0\}$, and $\mathbf{N^T}$ and $\mathbf{M^T}$ are the thermally induced contributions to the forces and moments.

$$\begin{aligned}
\mathbf{N^T} &= \begin{Bmatrix}N_x^T & N_y^T & N_{xy}^T\end{Bmatrix} = \Delta T\sum_{n=1}^{k}\overline{Q}_k\alpha_k\left(z_k - z_{k-1}\right) \\
\mathbf{M^T} &= \begin{Bmatrix}M_x^T & M_y^T & M_{xy}^T\end{Bmatrix} = \frac{\Delta T}{2}\sum_{n=1}^{k}\overline{Q}_k\alpha_k\left(z_k^2 - z_{k-1}^2\right)
\end{aligned} \tag{5}$$

dependent on the temperature change from cure ΔT, transformed stiffnesses of the k layers $\overline{Q}_k$, the thermal expansion coefficients α_k, and the through-thickness locations of the plies in the out-of-plane z-direction. Substituting the assumed form for the displacements and expanding the integral of Eq. (3) results in the following expression for the total strain energy,

$$W_{lam} = H_1\left(L_xL_y\right) + H_2\left(\frac{L_xL_y^3}{12}\right) + H_3\left(\frac{L_x^3L_y}{12}\right) + H_4\left(\frac{L_x^3L_y^3}{144}\right) + H_5\left(\frac{L_xL_y^5}{80}\right) + H_6\left(\frac{L_x^5L_y}{80}\right) \tag{6}$$

where the form of the equation has been selected to isolate terms which are dependent on the planform (L_x and L_y), and those which are dependent on the material properties and plate curvatures, simplified as the coefficients $H_{1\text{-}6}$. The in-plane shape coefficients $d_{1\text{-}11}$ can be expressed in terms of the out-of-plane coefficients a and b. Thus to identify the static equilibria we seek the values of the two remaining unknowns a and b which minimise the total strain energy. Solution of Eq. (7) therefore yields the static laminate shapes.

$$\frac{\partial W_{lam}}{\partial a} = \frac{\partial W_{lam}}{\partial b} = 0 \tag{7}$$

Small piezoelectric elements bonded to the laminate surface are included by summing their individual contributions to the total strain energy of the laminate. Since the piezoelectric elements are added post-cure they experience zero thermal gradient and thus the contribution to the strain energy is driven by the stiffness properties of each of the n elements,

$$W = W_{lam} + \sum_{n=1}^{p} \frac{1}{2} \int_{-Ly,mfc,n/2}^{Ly,mfc,n/2} \int_{-Lx,mfc,n/2}^{Lx,mfc,n/2} \begin{bmatrix} \mathbf{A_{mfc}} & \mathbf{B_{mfc}} \\ \mathbf{B_{mfc}} & \mathbf{D_{mfc}} \end{bmatrix} \begin{Bmatrix} \boldsymbol{\varepsilon}^0 \\ \boldsymbol{\kappa}^0 \end{Bmatrix} dxdy \tag{8}$$

Maintaining the assumption that Eq. (1) is a good approximation to the resulting static shapes, discussed in Section 3, Eq. (8) is substituted into Eq. (7) to identify the curved shapes of the piezoelectric-laminate device.

2.2 Static shapes of laminates of arbitrary planform

In this work we look to generalise the existing modelling above to consider arbitrary planforms. It is required that these laminates maintain the property of bistability and thus there are limits to the geometries which may be considered[5]. It is assumed that the static shapes of arbitrary geometry bistable laminates may still be approximated by the out-of-plane displacement profile of Eq. (1). In deriving a new expression for the laminate strain energy we note that given the form of Eq. (6), the coefficients $H_{1\text{-}6}$ are functions of material properties and curvatures a and b only and therefore remain unchanged for an arbitrary geometry. The geometric terms relating to the spatial integration in Eq. (3) must be derived for the arbitrary case. We begin by discretizing a rectangular design domain by a grid of rectangular elements as defined in Fig. 2.

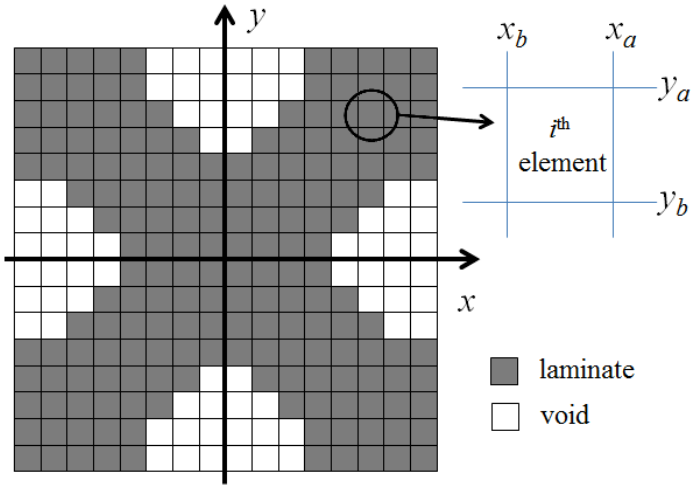

Figure 2. Discretisation of an example bistable laminate planform.

The strain energy of a single element within the domain can be defined as,

$$W = H_1\left(x_{ai} - x_{bi}\right)\left(y_{ai} - y_{bi}\right) + H_2 \frac{\left(x_{ai} - x_{bi}\right)\left(y_{ai}^3 - y_{bi}^3\right)}{3} + H_3 \frac{\left(x_{ai}^3 - x_{bi}^3\right)\left(y_{ai} - y_{bi}\right)}{3} + H_4 \frac{\left(x_{ai}^3 - x_{bi}^3\right)\left(y_{ai}^3 - y_{bi}^3\right)}{9} + H_5 \frac{\left(x_{ai} - x_{bi}\right)\left(y_{ai}^5 - y_{bi}^5\right)}{5} + H_6 \frac{\left(x_{ai}^5 - x_{bi}^5\right)\left(y_{ai} - y_{bi}\right)}{5} \tag{9}$$

where the subscript i refers to the i^{th} element. Summing the strain energy terms for all elements k within the domain results in,

$$W = \sum_{n=1}^{k} \eta_i \left[\begin{array}{l} H_1 (x_{ai} - x_{bi})(y_{ai} - y_{bi}) + H_2 \dfrac{(x_{ai} - x_{bi})(y_{ai}^3 - y_{bi}^3)}{3} + H_3 \dfrac{(x_{ai}^3 - x_{bi}^3)(y_{ai} - y_{bi})}{3} \\ + H_4 \dfrac{(x_{ai}^3 - x_{bi}^3)(y_{ai}^3 - y_{bi}^3)}{9} + H_5 \dfrac{(x_{ai} - x_{bi})(y_{ai}^5 - y_{bi}^5)}{5} + H_6 \dfrac{(x_{ai}^5 - x_{bi}^5)(y_{ai} - y_{bi})}{5} \end{array} \right] \tag{10}$$

where η is a $1 \times k$ vector of 1s and 0s defining which elements are present (1) within the arbitrary geometry and which are void (0). A full vector of 1s would therefore yield an identical result to Eq. (6), while a mix of 1s and 0s can be used to define any desired shapes with any density of grid. Finally, Eq. (10) is substituted into Eq. (7) and solved numerically to determine the static shapes of the arbitrary geometry laminate. The process of including piezoelectric elements, which remain rectangular in this paper due to manufacturing constraints but which could also have arbitrary shape, is identical to that in Eq. (8).

It is noted that given the form of Eq. (10) the location of the element relative to the geometric centre, as well as the area, is also crucial in determining its energy contribution, i.e. distributing the same amount of material in a long thin cantilever or a square plate will result in different total strain energy and thus different stable curvatures[15]. It is also noted that the density of the grid has no discernable effect on computation time as cured shapes are not solved on an element by element basis. A single shape function is used and thus no continuity conditions between elements are required. A very fine grid therefore provides a close approximation to a shape defined by a smooth boundary. The validity of these assumptions is presented in Section 3.

2.3 Mapping bistable laminates to a dynamics model

A model for square bistable composite laminates has previously been mapped to a dynamics model for base excitation[12]. The governing equations take the following form,

$$\begin{aligned} \mathbf{M}\ddot{\mathbf{x}} + \mathbf{D}\dot{\mathbf{x}} + \mathbf{K}(\mathbf{x}) + \theta \mathbf{V} &= \mathbf{F}(t) \\ C_p \dot{\mathbf{V}} + \frac{\mathbf{V}}{R_l} + \theta \dot{\mathbf{x}} &= 0 \end{aligned} \tag{11}$$

where $\mathbf{x} = [a, b]^T$, $\mathbf{M}$ is the mass matrix, $\mathbf{D}$ is the Rayleigh proportional damping matrix, $\mathbf{K}$ is the nonlinear restoring force defined for a double-well strain energy profile, θ is he piezoelectric coupling, $\mathbf{F}$ is the forcing term defining sinusoidal base excitation from the laminate centre, and $\mathbf{V} = [\mathrm{V}, \mathrm{V}]^T$ is the voltage across a load resistance R_l. The nonlinear restoring force is defined by noting that the strain energy of Eq. (6) can alternatively be expressed as fourth order polynomial of the following form,

$$W = g_1 a^2 b^2 + g_2 ab + g_3 a^2 + g_4 b^2 + g_5 a + g_6 b + g_7 \tag{12}$$

where $g_{1\text{-}7}$ are known functions of material properties and geometry. The derivative of Eq. (12) with respect to the plate curvatures gives the restoring force as a function of a and b,

$$\mathbf{K}(\mathbf{x}) = \frac{\partial W(a, b)}{\partial \mathbf{x}} \tag{13}$$

For arbitrary geometry laminates we adopt the same process, substituting Eq. (10) into Eq. (13) to map the restoring force for any arbitrary shape. The mass matrix must also be reformulated from that presented by Betts et al.[12] to account for the arbitrary distribution of the laminate material about the geometric centre. The mass matrix is defined such that $\mathbf{M}\ddot{\mathbf{x}}$ represents the work done by inertial forces. For a centrally clamped thin plate the work done takes the form[16],

$$\delta W_u = \rho h \int_A \ddot{w} \delta w dA \tag{14}$$

where an overdot indicates differentiation with respect to time, and the A is the area of the laminate. Substituting Eq. (1) into Eq. (14) results in,

$$\delta W_u = -\rho h \int_A \left(\ddot{a}x^4 + \ddot{b}x^2y^2\right)\delta a + \left(\ddot{b}y^4 + \ddot{a}x^2y^2\right)\delta b dA \tag{15}$$

Integrating over the laminate area as defined in Fig. 2 for an arbitrary geometry laminate results in,

$$\begin{aligned}\delta W_u = \sum_{i=1}^{n} & -\frac{1}{4}\rho h\left(\frac{\left(x_{ai}^5 - x_{bi}^5\right)\left(y_{ai} - y_{bi}\right)}{5}\ddot{a} + \frac{\left(x_{ai}^3 - x_{bi}^3\right)\left(y_{ai}^3 - y_{bi}^3\right)}{9}\ddot{b}\right)\delta a \\ & -\frac{1}{4}\rho h\left(\frac{\left(x_{ai} - x_{bi}\right)\left(y_{ai}^5 - y_{bi}^5\right)}{5}\ddot{b} + \frac{\left(x_{ai}^3 - x_{bi}^3\right)\left(y_{ai}^3 - y_{bi}^3\right)}{9}\ddot{a}\right)\delta b\end{aligned} \tag{16}$$

from which we extract the following mass matrix for the laminate alone,

$$\mathbf{M_{lam}} = \sum_{i=1}^{n} \frac{\rho h}{4}\begin{bmatrix} \dfrac{\left(x_{ai}^5 - x_{bi}^5\right)\left(y_{ai} - y_{bi}\right)}{5} & \dfrac{\left(x_{ai}^3 - x_{bi}^3\right)\left(y_{ai}^3 - y_{bi}^3\right)}{9} \\ \dfrac{\left(x_{ai}^3 - x_{bi}^3\right)\left(y_{ai}^3 - y_{bi}^3\right)}{9} & \dfrac{\left(x_{ai} - x_{bi}\right)\left(y_{ai}^5 - y_{bi}^5\right)}{5} \end{bmatrix} \tag{17}$$

It is noted that the mass matrix for the laminate is independent of the out-of-plane location of the individual plies. The contribution due to the addition of a number of piezoelectric elements can therefore be summed with Eq. (17) to give,

$$\mathbf{M} = \mathbf{M_{lam}} + \sum_{j=1}^{m}\sum_{i=1}^{n} \frac{\rho_{mfc} h_{mfc}}{4}\begin{bmatrix} \dfrac{\left(x_{j,ai}^5 - x_{j,bi}^5\right)\left(y_{j,ai} - y_{j,bi}\right)}{5} & \dfrac{\left(x_{j,ai}^3 - x_{j,bi}^3\right)\left(y_{j,ai}^3 - y_{j,bi}^3\right)}{9} \\ \dfrac{\left(x_{j,ai}^3 - x_{j,bi}^3\right)\left(y_{j,ai}^3 - y_{j,bi}^3\right)}{9} & \dfrac{\left(x_{j,ai} - x_{j,bi}\right)\left(y_{j,ai}^5 - y_{j,bi}^5\right)}{5} \end{bmatrix} \tag{18}$$

where m is the number of individual piezoelectric MFCs whose locations are defined by n elements in the same way as the laminate definition of Fig. 2.

Rayleigh proportional damping **D** is assumed of the form,

$$\mathbf{D} = \alpha\mathbf{M}\dot{\mathbf{x}} + \beta\mathbf{K}(\mathbf{x}) \tag{19}$$

where α and β are the mass and stiffness proportional coefficients. For the frequency range considered for energy harvesting the mass term dominates the damping. We therefore assume β to be zero. The mass term is defined as $\alpha = 4\pi\zeta\omega$ where ζ is the critical damping ratio determined at frequency ω. The decay response of oscillations of the harvester at the resonant frequency is experimentally measured by a laser vibrometer and used to determine ζ by the logarithmic decrement method[17]. Experimental values are discussed in Section 4.

The effective piezoelectric coupling coefficient[17] is defined as $\theta = \sqrt{(k_e^2 \mathbf{K} C_p)}$ where k_e^2 is the electromechanical coupling factor (0.48 for the material used in this work[18]) and C_p is the capacitance of the MFC.

Base excitation is introduced by the external forcing term **F** which takes the form $\mathbf{F} = \mathbf{M}\ddot{z}$ where the out-of-plane displacement of the shaker is assumed to take a sinusoidal form whose magnitude allows control of the peak acceleration.

3. EXPERIMENTAL VALIDATION OF STATIC ARBITRARY SHAPE MODELLING

To validate the proposed model we experimentally test a series of laminates of different planform. These laminates are all cut from 150×150mm square $[0/90]_T$ laminates (HTA/913c[19]) with different sections removed. Three laminates are cut to cruciform shapes (+ shape) with 20, 30 and 40% of the total square area removed, referred to from this point onwards as +20, +30 and +40. Three further laminates are cut to saltire shapes (× shape) with 20, 30 and 40% of the total square area removed, referred to from this point onwards as ×20, ×30 and ×40. These planforms have been selected to provide a variety of on-axis and off-axis curvatures, and incrementally deviate from the standard square shape towards a loss of bistability. All manufactured laminates are predicted to remain bistable by the model as two stable configurations

of locally minimized strain energy are identified in each case. Each laminate is laser cut from the manufactured square using a CAD template drawn to the exact required surface area as a cutting guide.

3.1 Bare laminates of arbitrary shape

We initially consider the validity of the arbitrary shape model in predicting the static cured shapes of bare laminates (no piezoelectric material) of arbitrary shape. A Digital Image Correlation (DIC) system is used to map the static laminate shapes of the six example laminates at high resolution (~70 data points/cm^2) and accuracy (50μm). The three-dimensional displacements of the laminates are captured by the DIC. This system uses two cameras in stereo to take images of a painted speckled pattern of the laminate surface. Comparing the speckled pattern in each of the two images with a reference frame allows determination of the three-dimensional locations across the surface. Figure 3 shows an example result for the out-of-plane displacement mapped across the surface of both stable shapes of the ×20 laminate, where red regions are closest to the camera and purple furthest away.

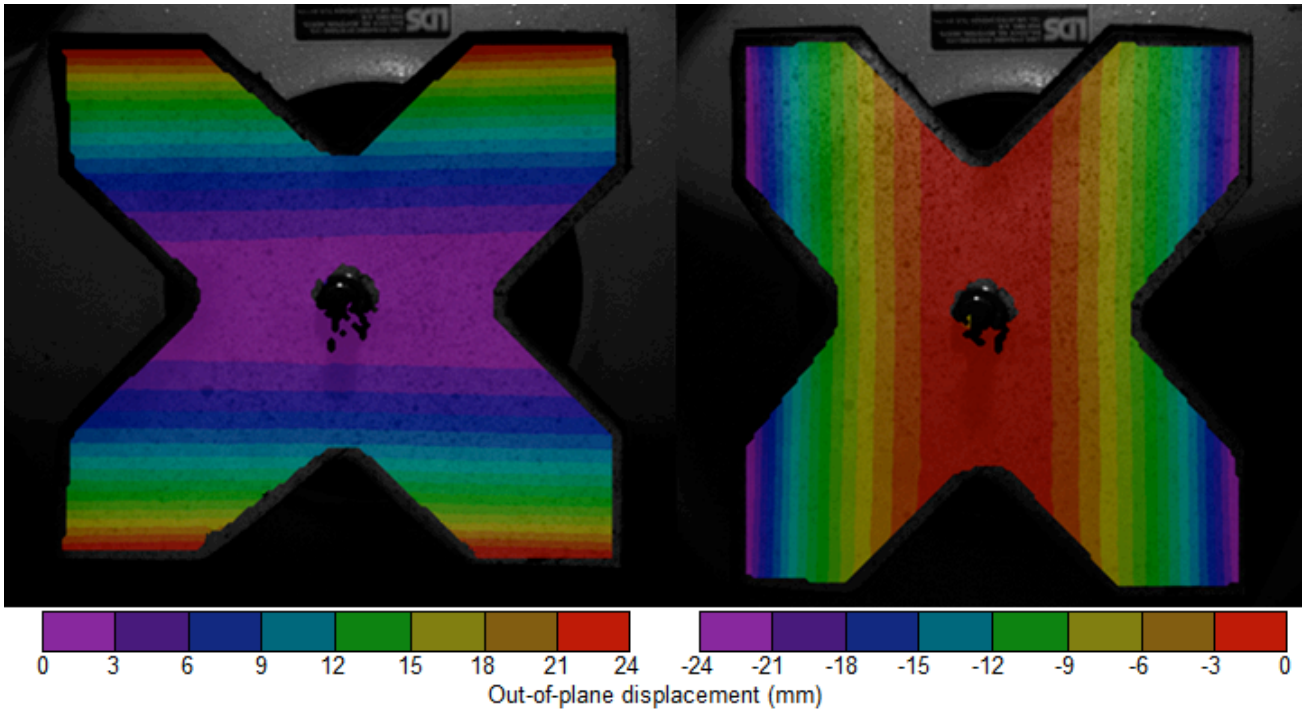

Figure 3. An example DIC result for the out-of-plane displacement of both stable shapes of the ×20 laminate. Red denotes displacements nearest the camera, purple furthest away.

This data is extracted from the DIC software for further analysis in Matlab. Each [x, y] coordinate pair in the undeformed x-y plane is substituted into Eq. (1) using the modelling predictions for the curvatures a and b determined by Eqs. (7) and (10). This produces a map of 13,187 [x, y, z] coordinates, each of which can be directly compared against the equivalent experimental value to produce a map of the errors between modelling and experiments. Figure 4a shows this comparison for the example ×20 laminate in terms of absolute distance (experimental – modelling), while Fig. 4b shows the value as a percentage of measured value. Note that in Fig. 4b the central region is omitted as the displacements become small compared with the accuracy of the experimental measurements (50μm).

The data in Fig. 4 is further analysed by plotting the data as histograms. The range of displacement in Fig. 4a is divided into 0.2mm intervals (Fig. 5a), and the range of percentages in Fig. 4b is divided into 0.5% intervals (Fig. 5b). For this laminate the mean and median displacement differences are 0.40mm ad 0.29mm respectively, or 5.49% and 5.23%. The highest percentage errors between modelling and experiments are localised at the laminate corners and reach a maximum of 15%. However, as shown by Fig. 5a these errors occur over a small percentage of the total laminate area with errors between 3 and 7% accounting for 86% of the total area.

Errors of the order 3-7% in the cylindrical shape are well within the bounds previously demonstrated for a square laminate model[20] and are within the range which can be attributed to uncertainty in material properties and manufacturing processes[21].

This experimental validation process is repeated for all six manufactured laminates. Table 1 presents a summary of the mean and median values of error between experimentally measured and predicted shapes for the six laminates in each of the two stable shapes. For each laminate there is one side with a slightly smoother surface than the other due to the manufacturing process; the smooth surface is associated with the laminate that is in contact with the tool surface during the curing process. Shape 1 is defined as having the smoothest surface on the concave side.

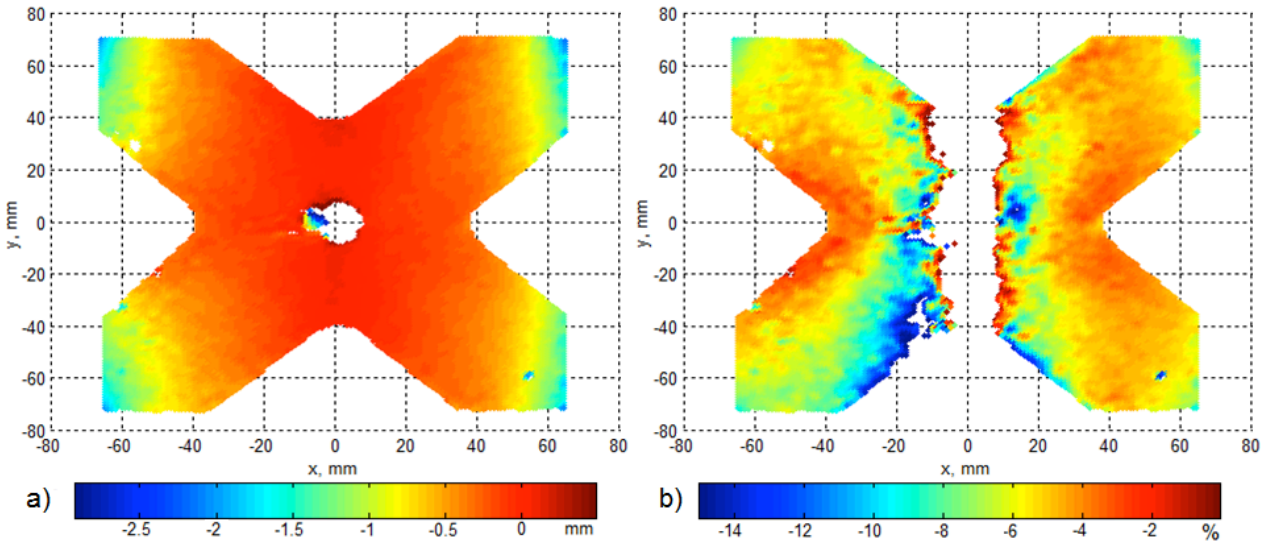

Figure 4. a) Difference between experimental and predicted shapes of the ×20 laminate in mm and b) as a percentage of the measured value.

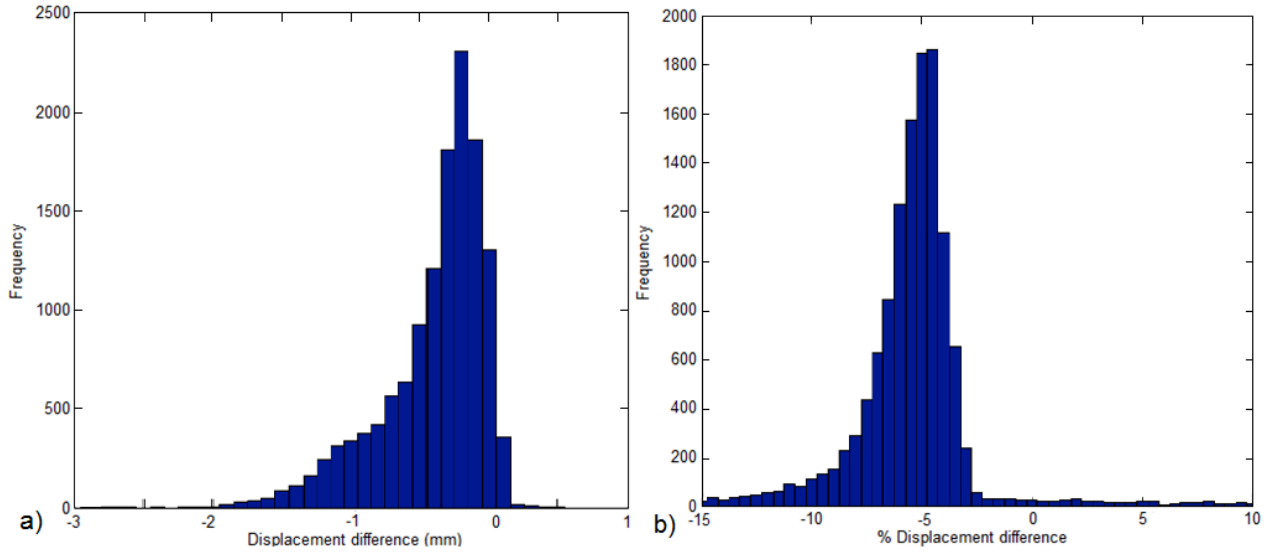

Figure 5. Histograms of a) displacement difference across the surface shown in Fig. 4a and b) percentage difference across the surface shown in Fig. 4b.

Table 1. Experimentally measured errors (experimental – modelling, negative values represent a modelling overestimate) across the surfaces of six arbitrary shape laminates.

	Error (Shape 1)		Error (Shape 2)	
	mm	%	mm	%

	mean	median	mean	median	mean	median	mean	median
×20	-0.399	-0.288	-5.449	-5.237	-0.499	-0.385	-7.446	-7.269
×30	-0.413	-0.330	-5.807	-5.366	-0.520	-0.462	-7.779	-7.626
×40	-0.422	-0.376	-6.004	-5.445	-0.533	-0.491	-7.894	-7.815
+20	-0.381	-0.243	-6.702	-6.302	-0.487	-0.364	-8.204	-8.033
+30	-0.256	-0.228	-5.427	-5.622	-0.359	-0.300	-7.315	-7.312
+40	-0.307	-0.149	-6.566	-6.202	-0.454	-0.288	-8.104	-7.955

For all laminates the mean percentage error is consistently 5-6% in Shape 1 and 7-8% for Shape 2. Shape 2 has the rougher surface on the concave side resulting in slightly reduced curvature relative to Shape 1. As this effect is not accounted for in the model the result is that errors are slightly larger (i.e. modelling is more of an over-estimate than for Shape 1). This ~2% change due to the rough surface correlates well with results previously published for square laminate model[20].

3.2 Addition of piezoelectric elements

Having demonstrated that the proposed model for the static shapes of arbitrary geometry laminates is valid within the error bounds previously observed for square laminates of the same layup, we consider the influence of attaching small piezoelectric elements to the laminate surface. Attachment of MFCs which do not cover the entire laminate surface introduces regions of higher stiffness which has the effect of localised flattening of the laminate curvature. In the proposed model the curved shape of the laminate is assumed to conform to the constant curvature approximation of Eq. (1) thus unable to model the local curvature change due to the introduction of a MFC. To investigate the effects of this simplification we experimentally measure the curved shape of a laminate with MFCs attached. The larger the area removed from the laminate the lower the amplitude of excitation required for snap-through. However, removal of larger areas also tends towards lower curvatures and eventually a loss of bistability. As the addition of MFCs further suppresses the curvatures the ×30 laminate is chosen for this test as a compromise to ensure that the energy harvester maintains bistability. Four MFCs of 28 × 14mm are attached in the locations highlighted in Fig. 6 by white rectangles. Figure 6 shows the out-of-plane displacement of the laminate with MFCs attached to the back surface where the purple contours are furthest away and red nearest to the camera. Firstly it is noted from the contour map of Fig. 6 that any localised flattening of the curvature is minimal as the curved profile maintains the approximately cylindrical shape seen for the bare laminate with no MFCs attached. Secondly we compare the displacement at the centre of each of the MFCs (6.9mm) with the value predicted by the model including MFCs (7.3mm), and the peak displacement at the corner of the laminate (18.5mm) with that predicted by the model (19.4mm). In both cases the error is of the order of 5-6% and is an overestimate as observed for the bare laminate. Attaching MFCs to one surface also has the effect of forming two stable states of different curvature. We therefore repeat the tests for the second stable state. The average measured displacement at the centre of the four MFCs is 6.4mm, compared with 6.0mm predicted by the model (7% overestimate), while the experimental peak displacement at the corners (14.7mm) and model prediction (16.0mm) are within 9%. We conclude that in both states the errors are within the same bounds as observed for the bare laminate.

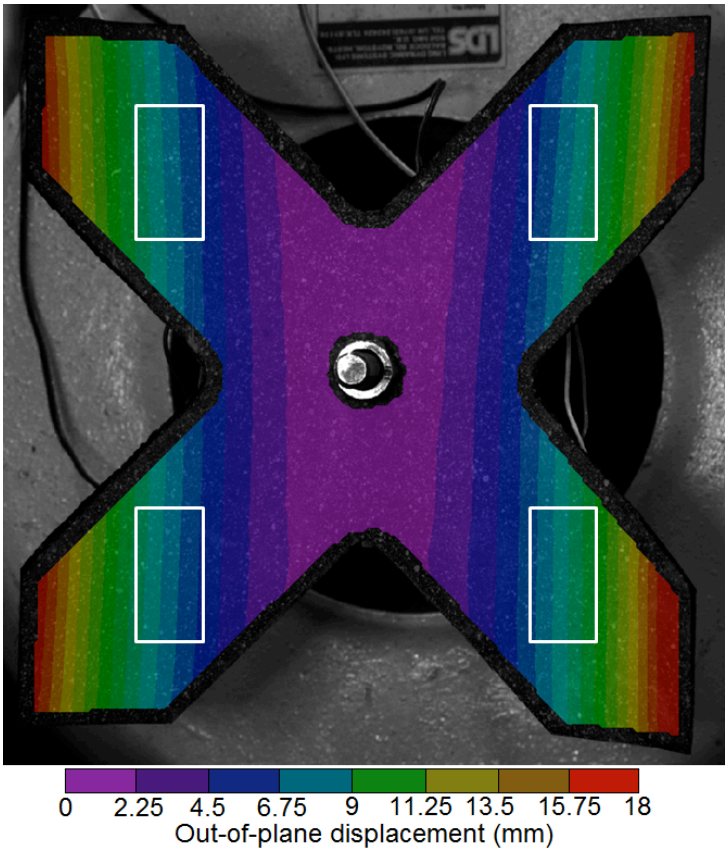

Figure 6. DIC result for the out-of-plane displacement of the ×30 laminate with four MFCs of 28 × 14mm bonded to the back surface in positions marked by white rectangles. Red denotes displacements nearest the camera, purple furthest away.

3.3 Modelling limitations

An additional result of the DIC characterisation is the identification of laminates with more than two stable configurations. When the individual sections of the × shape laminates become high in aspect ratio their fixed root near the centre of the laminate has sufficiently small effect that they can behave as an individual bistable element. This is demonstrated by Fig. 7 which shows two additional stable configurations of the ×40 laminate. Figure 7a shows a configuration where the top left and bottom left sections are snapped forward (are red), while Fig. 7b shows a configuration where the top left and bottom right sections are snapped forward (are red). These additional states are only noted for the ×40 laminate and represent finely balanced stable states requiring very little external energy input to return to the more common cylindrical configuration. Due to the assumed shape function of Eq. (1) these configurations are not predicted by modelling and thus care should be taken when applying the proposed model to extreme cases of laminate profile.

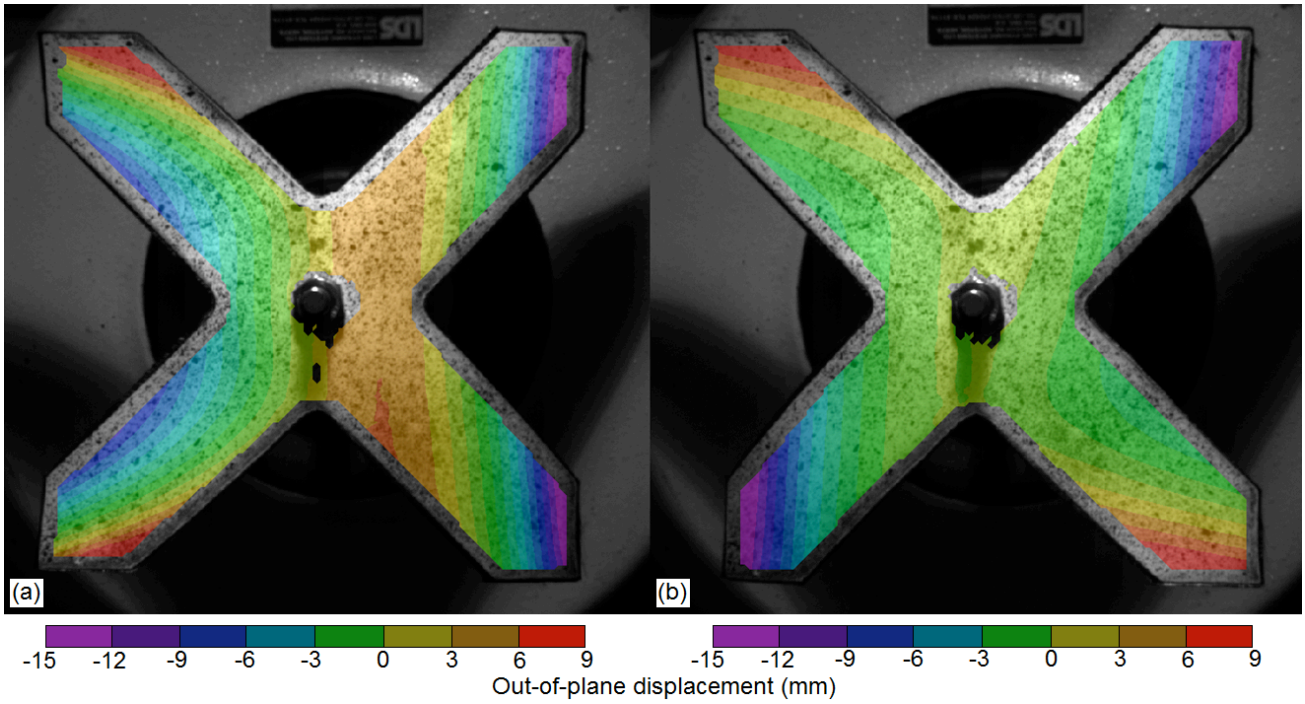

Figure 7. DIC results for the out-of-plane displacement of the ×40 laminate in two additional stable configurations (a) top left and bottom left sections are snapped forward and (b) top left and bottom right sections are snapped forward. Red denotes displacements nearest the camera, purple furthest away.

4. DYNAMIC RESPONSE OF ARBITRARY SHAPE LAMINATES FOR ENERGY HARVESTING

We select the ×30 laminate with four piezoelectric MFCs positioned as defined in Fig. 6 as an example arbitrary shape energy harvester to compare against the dynamics model. For experiments the harvester is attached at its centre to an electrodynamic shaker. The shaker input is generated in LabView and passed via a power amplifier. Frequency sweeps are performed such that the peak acceleration at the shaker attachment remains constant. This is achieved using a laser triangulation sensor monitoring the movement of the shaker, passing the information in a feedback loop and tuning the input amplitude until the desired level is met. In this study we measure the voltage output from one of the four MFCs only. The single MFC is attached across a load resistance box which is controlled via LabView to perform sweeps of load resistance. At each frequency and resistance setting the system is allowed to settle for 2 seconds and the root mean square of the voltage output (V_{rms}) is recorded. Power output from the single MFC is then determined by V_{rms}^2/R_l. The capacitance of the individual MFC is experimentally measured as C_p = 34nF and the mass proportional damping coefficient is experimentally determined by the method outlined in Section 2 to be $\alpha = 55.7$.

Figure 8 shows the experimental results recorded for frequency (26-50Hz) and resistance sweeps (10kΩ-1MΩ) performed at 3g peak acceleration (Fig. 8a) and 9g peak acceleration (Fig. 8b). The lower peak acceleration is selected to limit the behaviour to single-well only (i.e. no snap-through events) while the higher peak acceleration is selected to provide snap-through modes across a range of frequencies.

Considering first the 3g case (Fig. 8a) it is noted that a resonant peak is evident at approximately 34Hz with power outputs dropping dramatically either side of this peak. Simple impedance matching between the load resistance and the piezoelectric element ($R_l = 1/\omega C_p$) suggests that at 34Hz power should be a maximum at 138kΩ, correlating well with the experimentally observed peak at 124kΩ. Taking a cut through the surface plot at 124kΩ produces the plot of Fig. 9(a) were the dark grey boxes indicate the experimentally measured power outputs at 2Hz intervals. Also plotted as white boxes in Fig. 9(a) are the power outputs predicted by the model as outlined in Section 3 using the same frequency and resistance load conditions. It is noted that the predicted frequency at which the power is a maximum correlates well with experiments and shows a predicted power of 0.034mW compared with the measured value of 0.032mW. However,

it is also noted that the resonant peak is sharper in modelling than experiments, falling away more quickly either side of the peak than was experimentally observed. This suggests the model may be under-damped, and that the damping coefficient ($\alpha = 55.7$) used is too small.

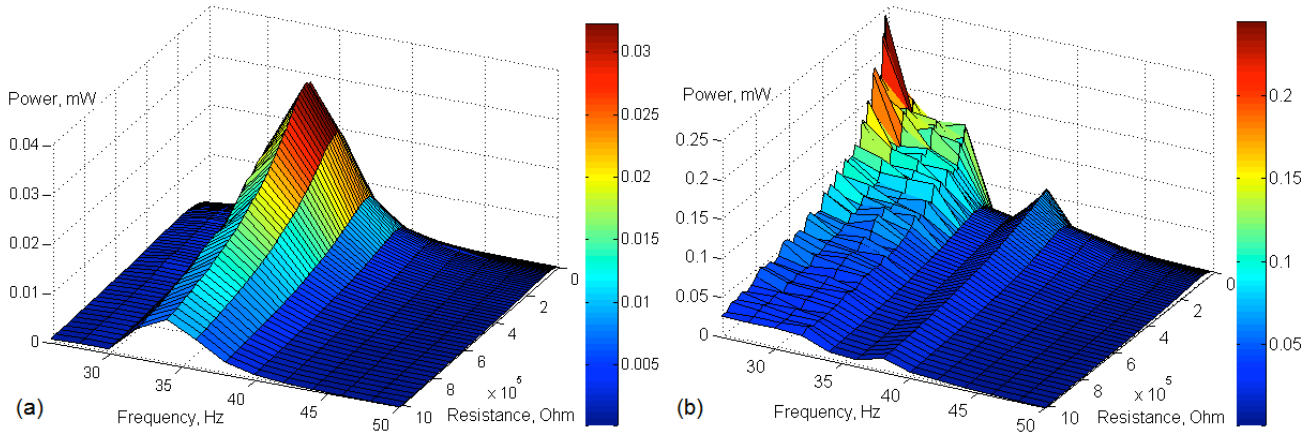

Figure 8. Experimental power outputs for a single MFC (one of four) attached to the surface of the ×30 laminate at (a) 3g peak acceleration and (b) 9g peak acceleration in the range 26-50Hz and 1kΩ-1MΩ.

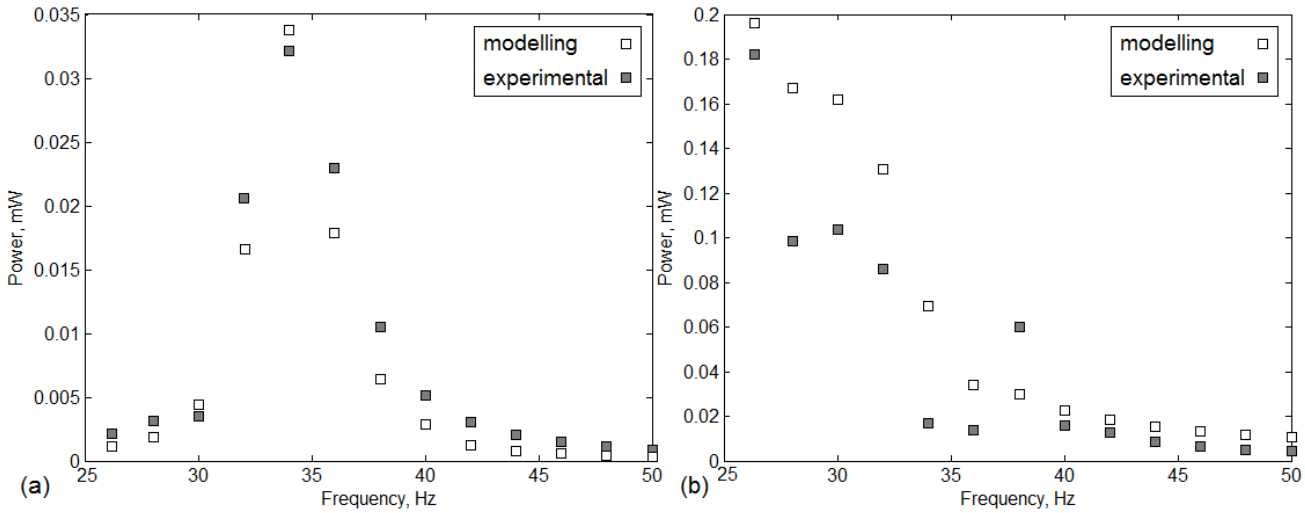

Figure 9. Experimental and modelling power outputs for a single MFC (one of four) attached to the surface of the ×30 laminate at (a) 3g peak acceleration and (b) 9g peak acceleration in the range 26-50Hz with resistance load of 124kΩ.

For the 9g condition Fig. 8(b), the peak powers are noted to be an order of magnitude higher than for the 3g test and are seen to shift to lower frequencies. In the range 26-34Hz the pattern of power outputs is less smooth compared to 3g. Within this range the laminate is experiencing double-well oscillations with frequent snap-through events. The spikes in the power are explained as the patterns of these snap-through events can be either periodic or chaotic and are highly sensitive to small changes in the vibration patterns. It is therefore difficult to select a power maximising resistance load from experimental data but the highest power output is seen at the same value (124kΩ) as in the 3g tests. We therefore select the same 124kΩ load to take a cut-through of the surface to produce Fig. 9(b). Again the experimental power outputs are plotted as dark grey boxes and the equivalent model prediction plotted as white boxes. In the higher frequency range 40-50Hz where behaviour is limited to a single well as in the 3g tests the modelling and experimental power outputs fall to below 0.02mW.. In the lower frequency range between 26-40Hz experimental peak power increases to 0.182mW (0.198mW for the model). However, larger discrepancies are observed between model and

experiments in this region and this is attributed to the sensitivity of the pattern of snap-through events in this region. At some frequencies within this range it is anticipated that a periodic snap-through pattern observed in experiments may be compared with a chaotic snap-through pattern predicted by modelling, for example. Despite these discrepancies in the power outputs when comparing snap-through behaviour at specific frequencies, the power outputs for single well behaviour (>40Hz in Fig. 9(b)) correlate well, as discussed for the 3g tests. The boundary between single-well and double-well behaviour, marked by a sharp rise in power in Fig. 9(b), is approximately 32Hz for experiments and 34Hz for the model, although a finer grid of data points is required to more accurately identify this boundary.

5. CONCLUSION

This paper presents the first analytical model of the cured shapes of laminates of asymmetric stacking sequence of arbitrary shape. Predictions of the cured shapes of bare laminates have been experimentally validated using a digital image correlation system for a series of laminates of differing non-square shape. Errors between modelling and experiments are shown to be within the bounds previous presented for square laminate modelling (5-7%). The analytical model is extended to include piezoelectric MFCs bonded to the laminate surface for energy harvesting applications. This static modelling is mapped to a dynamics model including electromechanically coupled behaviour and base excitation, and is used to compare against an experimental study of the energy harvesting performance of an example arbitrary geometry piezoelectric-laminate energy harvester. The dynamic model is shown to accurately capture the resonant frequency and power outputs for low acceleration, single-well behaviour, and to capture the frequency boundary at which snap-through behaviour occurs at higher accelerations. Large discrepancies in power output are noted in the range of frequencies at which snap-through occurs, attributed to the sensitivity of switching between different patterns of periodic and chaotic snap-through. The presented model is intended to provide a route to improving the design of piezoelectric-laminate energy harvesters for broadband operation, offering a large number of design variables for tailoring of the stiffness and mass distribution of the device.

REFERENCES

[1] Ju, S. H., Lin, H. T., and Huang, J. Y., “Dominant frequencies of train-induced vibrations,” Journal of Sound and Vibration, 319(1-2), 247-259 (2009).

[2] Zhu, Q., Guan, M., and He, Y., “Vibration energy harvesting in automobiles to power wireless sensors,” International Conference on Information and Automation Conference Proceedings, Shenyang China, 349-354 (2012).

[3] Wood, O. J., Featherston, C. A., Kennedy, D., Eaton, M., and Pullin, R, “Optimised vibration energy harvesting for aerospace applications,” Key Engineering Materials – Structural Health Monitoring II, 518, 246-260 (2012).

[4] Zhou, S., Cao, J., Erturk, A. and Lin, J, “Enhanced broadband piezoelectric energy harvesting using rotatable magnets”, Applied Physics Letters, 102(173901), 1-4 (2013)

[5] Hyer, M. W., “Calculations of the room-temperature shapes of unsymmetric laminates,” Journal of Composite Materials, 15(July), 296-310 (1981).

[6] Arrieta, A. F., Hagedorn, P., Erturk, A. and Inman, D. J., “A piezoelectric bistable plate for nonlinear broadband energy harvesting,” Applied Physics Letters, 97(10), 1-3 (2010).

[7] Betts, D. N., Kim, H. A., Bowen, C. R., and Inman, D. J., “The optimal configuration for broadband energy harvesting using bistable phenomenon,” Applied Physics Letters, 100(114104), 1-4 (2012).

[8] Betts, D. N., Kim, H. A., and Bowen, C. R., “Preliminary study of optimum piezoelectric cross-ply composites for energy harvesting,” Smart Materials Research, 2012(621364), 1-8 (2012).

[9] Dano, M. -L., and Hyer, M. W., “Thermally induced deformation behavior of unsymmetric laminates,” International Journal of Solids and Structures, 35(17), 2101-2120 (1998).

[10] Dano, M. -L., and Hyer, M. W., “SMA-induced snap-through of unsymmetric fiber-reinforced composite laminates”, International Journal of Solids and Structures, 40(22), 5949-5972 (2003).

[11] Ren, L., and Parvizi, A., “A model for shape control of cross-ply laminated shells using a piezoelectric actuator,” Journal of Composite Materials, 40(14), 1271-1285 (2006).

[12] Betts, D. N., Le Bas, P.-Y., Guyer, R., Bowen, C. R. and Kim, H. A., "A model for nonlinear bistable piezoelectric-laminate plates for broadband vibration energy harvesting", Smart Materials and Structures, Submitted (2014).
[13] Tawfik, S., Dancila, D. S. and Armanios, E., "Planform effects upon the bistable response of cross-ply composite shells", Composites Part A: Applied Science and Manufacturing, 42(7), 825-833 (2011).
[14] Arrieta, A. F., Bilgen, O., Friswell, M. I. and Ermanni, P., "Modelling and configuration control of wing-shaped bi-stable piezoelectric composites under aerodynamic loads", Aerospace Science and Technology, 29(1), 453-461 (2013)
[15] Jun, W. J., and Hong, C. S., "Effect of residual shear strain on the cured shape of unsymmetric cross-ply thin laminates," Composites Science and Technology, 38(1), 55-67 (1990).
[16] Diaconu, C. G., Weaver, P. M., and Arrieta A. F., "Dynamic analysis of bi-stable composite plates," Journal of Sound and Vibration, 322(4-5), 987-1004 (2009).
[17] Inman, D. J., [Engineering Vibrations], Pearson Education, Inc., Upper Saddle, NJ, 52-53 (2008)
[18] Smart Material Corp., www.smart-material.com/MFC-product-main.html, (Jan 2014).
[19] Giddings, P. F., Bowen, C. R., Kim. H. A. and Butler, R., "Characterisation of actuation properties of piezoelectric bi-stable carbon-fibre laminates", Composites Part A, 39(4), 697-703 (2008).
[20] Betts, D. N., Salo, A. I. T., Bowen, C. R. and Kim, H. A., "Characterisation and Modelling of the Cured Shapes of Arbitrary Layup Bistable Composite Laminates", Composite Structures, 92(7), 1694-1700 (2010).
[21] Brampton, C. J., Betts, D. N., Bowen, C. R. and Kim, H. A., "Sensitivity of bistable laminates to uncertainties in material properties, geometry and environmental conditions", Composite Structures, 102, 276-286 (2013).